



OPEN

Mid-infrared plasmonic inductors: Enhancing inductance with meandering lines

V́ctor Torres¹, Rubén Ortuño¹, Pablo Rodríguez-Ulibarri¹, Amadeu Griol², Alejandro Martínez², Miguel Navarro-Cía³, Miguel Beruete¹ & Mario Sorolla¹¹TERALAB (MmW-THz-IR & Plasmonics Laboratory), Universidad Pública de Navarra, 31006, Pamplona, Spain, ²Nanophotonics Technology Center, Universitat Politècnica de València, 46022, Valencia, Spain, ³Optical and Semiconductor Devices Group, Department of Electrical and Electronic Engineering, Imperial College London, SW7 2BT, London, UK.

We present a mid-infrared inductor that when applied to an extraordinary transmission hole array produces a strong redshift of the resonant peak accompanied by an unprecedented enlargement of the operation bandwidth. The importance of the result is twofold: from a fundamental viewpoint, the direct applicability of equivalent circuit concepts borrowed from microwaves is demonstrated, in frequencies as high as 17 THz upholding unification of plasmonics and microwave concepts and allowing for a simplification of structure design and analysis; in practical terms, a broadband funnelling of infrared radiation with fractional bandwidth and efficiency as high as 97% and 48%, respectively, is achieved through an area less than one hundredth the squared wavelength, which leads to an impressive accessible strong field localization that may be of great interest in sensing applications.

Recently, a great interest on the potential of plasmonics to enhance mid-infrared sources, sensors and detectors for applications like chemical sensing, thermal imaging and heat scavenging has emerged¹. Plasmonics took off by the end of the 20th century after the influential paper by Ebbesen *et al.*² where extraordinary transmission (ET) through small apertures was demonstrated, leading to the so-called “plasmonic resurrection”³. A full understanding of the physical mechanism underlying plasmonics is provided by the paradigm of complex waves⁴, i.e. waves with mutually orthogonal amplitude and phase planes. This kind of waves permits to unify the interpretation of plasmonic-like phenomena in different frequency ranges: leaky-plasmons or surface-plasmons at optics¹ and classical leaky waves or surface-waves⁵ (coined recently spoof plasmons⁶) at microwaves.

The complex waves paradigm opens immediately the application of the useful microwave toolbox at full, in particular, equivalent circuits. They were initially proposed for low frequency electronics⁷ and were generalized after the seminal paper by Schelkunoff⁸ to describe plane wave propagation as a transmission line problem, where discontinuities are lumped reactive elements⁹, widening ultimately the applicability of equivalent circuits up to the far infrared¹⁰. Plasmonics¹¹ research, hence, benefits today from both solid state physics and circuit concepts. However, it was common practice to explain plasmonic phenomena initially in terms of dimmers, molecules, coupled resonant states, and so on, even though it is satisfactorily explained with classical electromagnetism theory. This tendency is nowadays evolving and, for instance, infrared circuits - dubbed metatronics¹²⁻¹⁴ - are explained in terms of lumped elements and other plasmonic nanocircuits are designed making use of microwave circuit concepts such as characteristic impedance and transmission line theory^{15,16}. Equivalent circuit analysis applied to plasmonic structures has served to put the limits for genuine plasmonics, giving additionally an electrical circuit description for bulk plasmons, single-surface plasmons, and parallel-plate plasmons¹⁷. Also, equivalent circuits have been employed to satisfactorily describe ET^{18,19}. These analyses served to unify the different manifestations of ET resonance all along the electromagnetic spectrum, from millimetre-waves/terahertz^{5,20} to visible² where metals admit very different models, either finite conductivity or classical Drude model⁴ (as is customarily done in plasmonics), and allowed to engineer the ET resonance²¹.

Here, expanding ideas from microwaves, such that an inductance exists wherever a current loop resides, we demonstrate experimentally a terahertz inductor in frequencies as high as 17 THz by using meander-lines in a canonical ET hole array. Furthermore, rather than simply modelling the response of the metallic mesh from a

SUBJECT AREAS:

METAMATERIALS

ELECTRICAL AND ELECTRONIC
ENGINEERINGELECTRONIC PROPERTIES AND
MATERIALS

Received

24 September 2013

Accepted

10 December 2013

Published

7 January 2014

Correspondence and
requests for materials
should be addressed to
M.B. (miguel.beruete@unavarra.es)



circuital point of view, as it has been done before^{10,18,19}, we synthesize and engineer the response of ET hole arrays loaded with inductors of different turns from a metatronics perspective¹². We demonstrate that a strong frequency shift and a wider bandwidth appear even for a 1-turn inductor. This approach also allows us to quantify straightforwardly the inductance of the meander-line. The proposed inductance could be used as a building block for sophisticated devices in the THz and mid-infrared regimes, finding potential application in imaging or sensing among others¹.

Results

Three ET hole arrays loaded with 3-, 1- and 0-turn meander-lines were fabricated in order to experimentally validate the prospects of extending microwave theory to infrared frequencies. The samples were etched on a silicon (Si) wafer following the fabrication steps, detailed in Methods, covering an area of $5 \times 5 \text{ mm}^2$. The scanning electron microscopy (SEM) photograph of Fig. 1a shows the fabricated 3-turn meandering line hole array. The lower insets from left to right present the patterns unit cell of the 0-, 1-, and 3-turn meanders, where all prototypes were milled with the same hole and meander's width dimensions. The relevant structural dimensions and the different material layers that form the samples are given in the right upper inset. A 5 nm-thick chromium layer was deposited just for gold bonding purposes. The reason for choosing rectangular lattice arrays with a dense periodicity in one of the directions is due to their efficiency in the experimental verification of ET compared to square arrays²².

Experimental measurements were performed in the vacuum chamber of a Fourier-transform infrared spectrometer (FTIR) equipped with an optical bench and a He-cooled bolometer detector. A linear polarizer is used to excite the structure with vertical polarization. Horizontal polarization is neglected because the main aim of this work is to evaluate the influence of the meander lines on the spectral response. Vertical polarization is the one that allows the meanders to get excited by the induced current running along them. If the polarization is rotated, marginal currents will flow through the meander but this is out of the scope of this paper. Experimental results normalized with respect to the transmission through a bare silicon wafer can be seen in Fig. 1b for all prototypes. The resonance frequency corresponds to that at which the impinging light couples to a symmetric leaky mode thanks to the additional momentum provided by the lattice^{20,21,23}. This peak of transmission undergoes a significant redshift (around 21.57% and 39.65% for 1- and 3-turns with respect to 0-turn, respectively) along with a broadening of the operation bandwidth as the number of meander turns increases. Specifically, the fractional bandwidth defined as $\text{FBW} = (\omega_H - \omega_L)/\omega_C$ (where $\omega_H - \omega_L$ is the frequency range within which the spectral density is above half its maximum value and ω_C is the center operation frequency) is 3.85%, 40.45% and 96.62% for 0-, 1- and 3-turn meander-lines. This behavior is related to the effective inductance introduced by the meander-lines as it will be discussed next. A maximum infrared radiation efficiency of 47.56% is obtained for the 3-turns design through an area as small as $(\lambda_0/12.83)^2$ where λ_0 corresponds to the wavelength of the resonance frequency. Numerical results corresponding to best fits based on estimated dimensions from SEM pictures of the samples are also shown in Fig. 1b. Gold (chromium) was modeled following a Drude model with plasma frequency, $\omega_p = 1.196 \times 10^{16}$ (6.6942×10^{15}) rad/s and collision frequency $\omega_r = 8.0519 \times 10^{13}$ (7.1408×10^{13}) rad/s²⁴. The slight disagreement between experiment and numerical calculations can be attributed to the fact that metal properties are altered by nanocarves, since it is well known that nanostructured metals behave differently than in bulk²⁵.

Discussion

The physical mechanism underlying the meandering line hole array operation can be easily understood by means of circuit theory where

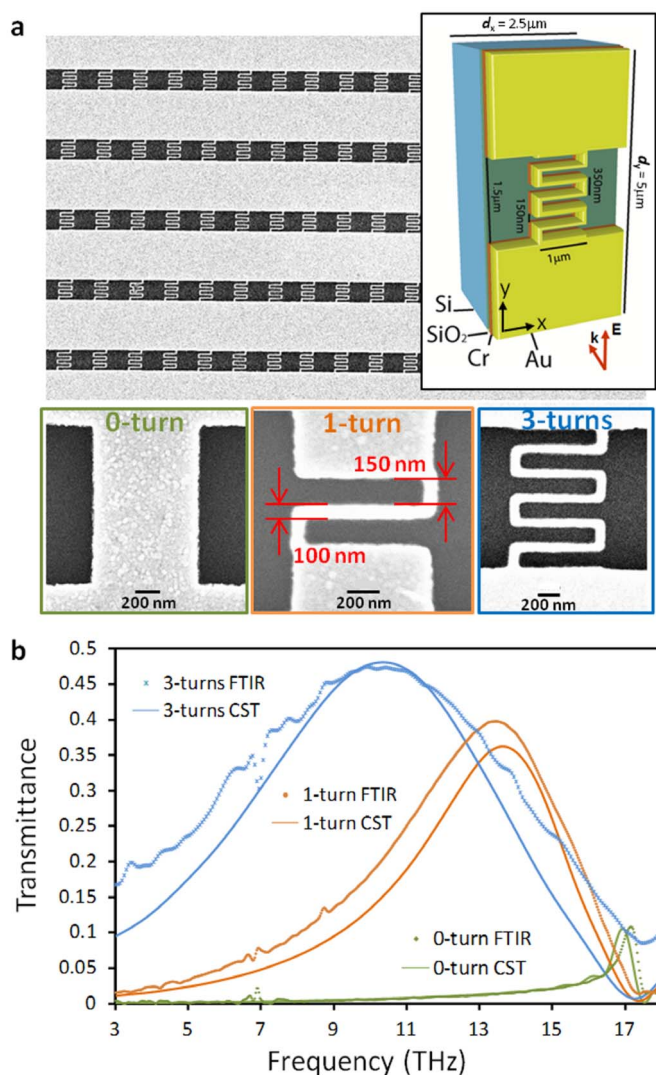


Figure 1 | SEM photographs of the prototypes and numerical vs. experimental results. (a), SEM photograph of the fabricated 3-turns meandered hole array. Lower insets from left to right show detailed photographs of the pattern unit cell of the 0-, 1-, and 3-turn meanders. Right upper inset depicts the structural dimensions and the different material layers that form the samples. (b), Numerical (CST) vs. experimental (FTIR) results of the field transmission for the 0-, 1-, and 3-turn designs.

the circuit elements are extracted from a straight physical interpretation of the hole array electrostatics. To extract rigorously the inductance of the aperture, the induced-surface current that flows on the metal and the magnetic flux generated by this current are calculated numerically (see Methods). As illustrated in Fig. 2a for the 0-turn design, each aperture behaves as a pair of virtual current loops (VCLs): the total induced surface-current (I_T) divides in two identical branches, each one carrying $I_B = I_T/2$ and flowing on the metal around each side of the aperture, which produce a magnetic flux through the aperture plane; the surface current is closed by a displacement current through the aperture (due to symmetry considerations, exactly in the middle of the aperture the magnetic field is null). Thus, the inductive nature of the aperture is modelled as two inductances L_B in parallel, leading to a total aperture inductance of $L_B/2$. Applying directly classical electrostatics²⁶, the magnetic flux is defined as^{27,27}:

$$\Phi_B = \mu_0 \iint_S \vec{H} d\vec{S} \quad (1)$$

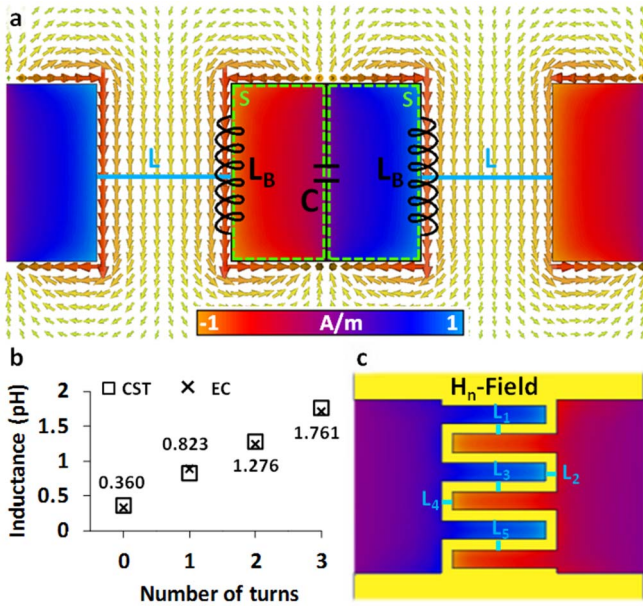


Figure 2 | Inductance extraction by means of the magnetic field and induced surface currents. (a), Normal component of the magnetic field (in color) and induced surface currents (arrows) when the structure is excited with a normal incident plane wave with the electric field oriented vertically. The interpretation of the inductances is shown explicitly. L_B models the inductance of each current branch around the aperture and C the admittance of the below-cutoff TM modes excited at the discontinuity plane. S (dashed green) depicts the surface taken for the integration of the magnetic flux of each VCL and L (solid blue) the closed line to compute the total induced surface current. (b), Inductance values obtained numerically (squares) and after optimization with the equivalent circuit model (crosses). (c), Normal component of the magnetic field (H_n -Field) for the 3-turns design where the magnetic field concentration in the meander's interstices is shown. For the meander-turns, several lines are evaluated to compute the total induced current. For the 3-turns design the lines are depicted as L_1 to L_5 . (a, c) share the same color bar.

calculated over the surface enclosed by one VCL, i.e. half the aperture area, represented as a green dashed line in Fig. 2(a); μ_0 is the permeability of free space and \vec{H} is the magnetic field. The surface current on the metal for one branch, by Ampère-Maxwell's law, is:

$$I_B = \frac{I_T}{2} = \frac{1}{2} \oint_L \vec{H} d\vec{l} \quad (2)$$

where L is a closed line orthogonal to the current path rounding the metallization (represented as blue in the figure). Thus, the total aperture inductance is:

$$L_{ap} = \frac{L_B}{2} = \frac{\Phi_B}{2I_B} \quad (3)$$

To extract the inductance, the calculations are done at very low frequency where the lumped elements from classical circuit theory are defined. Moreover, at such frequencies, the structural dimensions are much smaller than the wavelength, so propagation effects can be neglected. Thus, an instantaneous magnetic field can be assumed²⁷ and therefore Ampère-Maxwell's law is applied with small error.

The total inductance for 0-, 1-, 2- and 3-turns meandering line hole array is shown in Fig. 2b, where the increment of the total inductance with the number of turns is observed. This trend stems from the two main effects brought by the meander's turns: from

one side, an enhancement of the magnetic field at the meander's interstices (Fig. 2c), as expected from Faraday's law, and from the other side, a rise of the area enclosed by the VCL. Both effects boost the magnetic flux, and so L_{ap} , as the induced-surface current keeps constant despite the meander's turns increase. Approximately, each turn adds 0.45 pH. This increment is roughly linear since each additional meander turn can be seen as a new inductance in series with the previous one. Displacement currents appear at the meander's interstices, although in a first order approximation they can be neglected because, in the frequency range of interest, the inductive behavior dominates over the capacitance associated to them. However, the displacement current grows with frequency, and hence, one must consider the capacitance C related to the electrical energy in excess associated with below-cutoff TM modes excited at the discontinuity planes^{18,19}. For TM polarization and under normal incidence the relevant higher order Floquet-mode that takes part in ET resonance is the TM_{01} , whose capacitance is:

$$C^{(i)}(\omega) = \frac{A_{TM} k^{(i)}}{\omega Z^{(i)} \sqrt{\left(\frac{2\pi}{d_y}\right)^2 - (k^{(i)})^2}} \quad (4)$$

where $Z^{(i)} = \sqrt{\mu_0 / (\epsilon_0 \epsilon_r^{(i)})}$ is the background material characteristic impedance and $k^{(i)} = \omega \sqrt{\mu_0 \epsilon_0 \epsilon_r^{(i)}}$ is the propagation constant of the incoming wave; ϵ_0 is the permittivity of free space and $\epsilon_r^{(i)}$ is the relative permittivity of the medium ($i = air$ or Si); d_y is the length of the unit cell in the direction of the incident electric field and A_{TM} accounts for the degree of excitation of the TM_{01} mode at the interfaces. The losses owing to the interaction of the electromagnetic fields on the metal surface are modelled as a dispersive complex impedance $Z_c(\omega) = R_c(\omega) + j\omega L_c(\omega)$ defined as²⁸:

$$Z_c(\omega) = R_c(\omega) + j\omega L_c(\omega) = \eta_0 (1-j) \sqrt{\left(\frac{\omega\omega_r}{2\omega_p^2}\right) \left(1 - j\frac{\omega}{\omega_r}\right)} \quad (5)$$

where $\eta_0 = 377 \Omega$ is the intrinsic impedance of vacuum. For the finite area of the unit cell, this surface impedance is multiplied by d_y/d_x . Finally, in order to take into account the thickness of the metal and thus, the reactive energy stored inside the aperture, the resulting meander's equivalent circuit (Fig. 3a) is refined by adding a π -network of inductances¹⁸ $L_p - L_s - L_p$. Hence, the total inductance L_{ap} and the complex impedance Z_c split in two, one for each face of the metal.

Once the final model is established, the numerically found inductance values are introduced in the circuit and an optimization process is launched subsequently. The inductance obtained with the optimizer agrees well with that obtained with the numerical simulation, see Fig. 2b. The accuracy of the equivalent circuit is validated in Fig. 3b, where the transmission is shown, by comparing it against the numerical simulation. It is evident the good agreement between both results demonstrating the physical meaningful circuit representation. Therefore the frequency shift can be explained in terms of an increment of the total inductance: approximating equation (4) as a constant capacitance and assuming zero-thickness for simplicity (so the equivalent circuit is a simple RLC tank), the ET resonance happens at the RLC tank

resonance frequency $\omega_0 = \sqrt{\frac{1}{LC} - \left(\frac{R_c}{L}\right)^2}$, where the imaginary

admittance component vanishes, with L the serial sum of the aperture inductance L_{ap} and the internal surface impedance L_c . With the same approximation, the fractional bandwidth can be easily calculated:

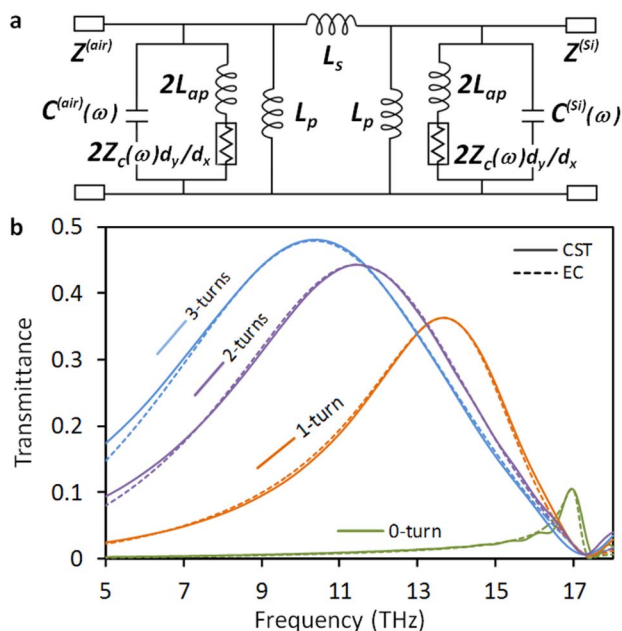


Figure 3 | Schematic and results of the equivalent circuit model. (a), Physical meaningful equivalent circuit model. $Z^{(air)}$ and $Z^{(Si)}$ are the background material characteristic impedance. L_{ap} models the aperture inductance, $Z_c^{(air)}(\omega)$ the losses in the metal and $C^{(air)}(\omega)$ and $C^{(Si)}(\omega)$ the admittance of the below-cutoff TM_{01} mode excited at the air-metal and metal-silicon interface, respectively. The π -network of inductances $L_p - L_s - L_p$ accounts for the thickness of the structure. (b), Field transmission results computed numerically (CST - solid lines) and via the equivalent circuit (EC - dotted lines).

$$FBW = \frac{R_c + \frac{(1 + \sqrt{\epsilon^{(Si)}}) L}{Z^{(air)}}}{\sqrt{\frac{L}{C} - R_c^2}} \quad (6)$$

where the bandwidth increment with \sqrt{L} is easily inferred.

It is worth remarking that total transmission is not obtained due to the impedance mismatch between air and silicon interfaces⁷. As a final remark, notice that despite the fundamental aperture mode depends on the number of meander turns, we checked numerically using the mode calculator of CST Microwave Studio that it remains at cutoff for all designs, and thus within the realm of ET. Hence, the transmission showed by the subwavelength apertures is surely ascribed to ET phenomena.

In conclusion, we demonstrate experimentally the synthesis of a meander-line inductor working at 17 THz borrowing ideas from microwave theory. The inductance increment with the number of meander-turns is due to an increment of the magnetic field at the meander's interstices. This increment is proved numerically following classical electrodynamics and validated by means of an equivalent circuit analysis, demonstrating the physical meaningful circuit representation at the mid-infrared frequency band. Therefore, this technique may suggest new ways of understanding circuits at infrared, although all electromagnetic considerations should be carefully taken in each design. These results can bring exciting prospects in new infrared devices based on classic designs at lower frequencies opening new application possibilities and merging the gap between microwave and infrared frequencies. Specifically, here we obtain experimentally an unprecedented mid-infrared redshift of 39.65% and a fractional bandwidth of 96.62% for the ET peak with a 3-meander-turns design. Furthermore, an infrared radiation efficiency of 47.56% is obtained together with strong magnetic field localization

Table 1 | Initial/final values of the optimized elements

N	L_{ap} (pH)	L_p (pH)	L_s (pH)	$A_{TM}^{(air)}$	$A_{TM}^{(Si)}$
0	0.360/0.330	0.5/0.160	0.1/0.097	1/1.36	1/0.65
1	0.823/0.886	0.5/0.395	0.1/0.084	1/1.91	1/1.23
2	1.276/1.241	0.5/1.035	0.1/0.096	1/2.18	1/1.41
3	1.761/1.710	0.5/1.392	0.1/0.106	1/2.40	1/1.43

that can be very useful to improve infrared devices for sensing or imaging application.

Methods

Numerical simulation. Full-wave Floquet-modes simulations were performed with the commercial software CST Microwave StudioTM. Unit Cell (Floquet) boundaries conditions were set and ten Floquet-modes were considered. The system solver accuracy chosen, in terms of the relative residual norm, was $1e^{-12}$. An adaptive tetrahedral mesh was used with convergence criteria of 0.01 over the zero-order transmission coefficient parameter. The meander turns were meshed further than the rest of the unit cell with a mesh step of $\lambda_{max}/100$ in order to obtain accurate results where λ_{max} corresponds to the wavelength of the maximum simulated frequency (18 THz).

Equivalent circuit analysis. The equivalent circuit results were obtained with the software Agilent Advanced Design SystemTM. The extraction of the equivalent circuit parameters was done with an optimization process from a few frequency points of the numerical simulations: three points from around the peak frequency and two points from low frequency. The optimizer parameters were set to use a Least-Square error-function and a random search method, where the inductance L_{ap} obtained with the numerical analysis was used as the seed for the optimization. L_s , L_p and A_{TM} are also optimized where the initial values are derived from our previous experience in equivalent circuits. Table 1 shows the initial/final values of the optimized elements.

Sample fabrication. The fabrication process was based on an optimised electron beam lithography step combined with a lift-off process. The first step consisted in the deposition of three consecutive PMMA950K positive resist layers to achieve a 270 nm resist height coating a silicon wafer. This resist was then exposed by means of a Raith150 e-beam system at 10 KeV with an aperture of 30 μ m. After optimization, the resist doses were 85 μ Q/cm² for areas and 735 pQ/cm for open paths forming the meanders structures. Then, the exposed pattern was transferred into the resist. The next step consisted in the evaporation of 100 nm of gold prior to lift-off process carried out with N-Methylpyrrolidone (NMP) as solvent at a pressure of 100 bars. After the lift-off process the gold meander patterns were obtained on the silicon substrates. Meander patterns with different unit cells were obtained as can be seen in Fig. 1a.

Measurement procedure. The measurement equipment used in the experiment was a Bruker Optics Vertex 80 v FTIR spectrometer. This spectrometer covers a wide bandwidth from the far infrared up to the ultraviolet. It is based on Fourier Transform of the infrared time signal. The interferogram is obtained by directing the infrared light emitted from the source (Globar in this case) to an interferometer that modulates the light. Afterwards, the signal passes through the sample under test placed in an additional optical bench attached to the instrument, eventually focusing the transmitted beam on the He-cooled bolometer detector. These measurements have been done in vacuum in order to avoid spurious absorption peaks due to air (water vapour, carbon dioxide among other gases). A resolution of 4 cm^{-1} was considered, with 16 scans per measurements to get the averaged spectrum and a scanning velocity of the interferometer moving mirror set to 2.5 kHz.

- Stanley, R. Plasmonics in the mid-infrared. *Nature Photon.* **6**, 409–411 (2012).
- Ebbesen, T. W., Lezec, H. J., Ghaemi, H., Thio, T. & Wolf, P. A. Extraordinary optical transmission through sub-wavelength hole arrays. *Nature* **391**, 667–669 (1998).
- Editorial, Surface Plasmon Resurrection, *Nature Photon.* **6**, 707 (2012). (doi:10.1038/nphoton.2012.276).
- Ishimaru, A. *Electromagnetic Wave Propagation, Radiation, and Scattering* (Prentice Hall, New Jersey, 1991).
- Beruete, M. et al. Enhanced millimeter-wave transmission through subwavelength hole arrays. *Opt. Lett.* **29**, 2500–2502 (2004).
- Pendry, J. B., Martín-Moreno, L. & García-Vidal, F. J. Mimicking Surface Plasmons with Structured Surfaces. *Science* **305**, 847 (2004).
- Ramo, S., Whinnery, J. R. & Van Duzer, T. *Fields and Waves in Communication Electronics* (Wiley, New York, 1994).
- Schelkunoff, S. A. The Impedance Concept and its Application to Problems of Reflection, Refraction, Shielding, and Power Absorption. *Bell Syst. Tech. J.* **17**, 17–48 (1938).
- Marcuvitz, N. *Waveguide Handbook* (McGraw-Hill, London, 1986).



10. Ulrich, R. Far-infrared properties of metallic mesh and its complementary structure. *Infrared Phys.* **7**, 37–55 (1967).
11. Maier, S. A. *Plasmonics: Fundamentals and Applications* (Springer, New York, 2007).
12. Engheta, N. Circuits with light at nanoscales: optical nanocircuits inspired by metamaterials. *Science* **317**, 1698–1702 (2007).
13. Sun, Y., Edwards, B., Alù, A. & Engheta, N. Experimental realization of optical lumped nanocircuits at infrared wavelengths. *Nature Mater.* **11**, 208–212 (2012).
14. Monticone, F., Estakhri, N. M. & Alù, A. Full Control of Nanoscale Optical Transmission with a Composite Metascreen. *Phys. Rev. Lett.* **110**, 203903 (2013).
15. Veronis, G. & Fan, S. Bends and splitters in subwavelength metal-dielectric-metal plasmonic waveguides. *Appl. Phys. Lett.* **87**, 131102 (2005).
16. Kocabas, S. E., Veronis, G., Miller, D. A. B. & Fan, S. Transmission line and equivalent circuit models for plasmonic waveguide components. *IEEE J Sel. Top. Quant.* **14**, 1462 (2008).
17. Staffaroni, M., Conway, J., Vedantam, S., Tang, J. & Yablonovitch, E. Circuit analysis in metal-optics. *Phot. Nano. Fund. Appl.* **10**, 166–176 (2012).
18. Medina, F., Mesa, F. & Marqués, R. Extraordinary transmission through arrays of electrically small holes from a circuit theory perspective. *IEEE T. Microw. Theory* **56**, 3108–3120 (2008).
19. Beruete, M., Navarro-Cía, M., Kuznetsov, S. A. & Sorolla, M. Circuit approach to the minimal configuration of terahertz anomalous extraordinary transmission. *Appl. Phys. Lett.* **98**, 014106 (2011).
20. Kuznetsov, S. A. *et al.* Regular and anomalous extraordinary optical transmission at the THz-gap. *Opt. Express* **17**, 11730–11738 (2009).
21. Beruete, M., Navarro-Cía, M., Torres, V. & Sorolla, M. Redshifting extraordinary transmission by simple inductance addition. *Phys. Rev. B* **84**, 075140 (2011).
22. Beruete, M. *et al.* Extraordinary transmission and left-handed propagation in miniaturized stacks of doubly periodic subwavelength hole arrays. *Opt. Express* **15**, 1107–1014 (2007).
23. Ulrich, R. Modes of propagation on an open periodic wave-guide for the far infrared. *Proceedings of the Symposium on Optical and Acoustical Micro-Electronics*, 359–376 (Polytechnic Press, New York, 1974).
24. Rakić, A. D., Djurišić, A. B., Elazar, J. M. & Majewski, M. L. Optical properties of metallic films for vertical-cavity optoelectronic devices. *App. Optics* **37**, 5271–5283 (1998).
25. Lloyd-Hughes, J. & Jeon, T.-I. A Review of the Terahertz Conductivity of Bulk and Nano-Materials. *J. Infrared Millim. Waves* **33**, 871–925 (2012).
26. Jackson, J. D. *Classical Electrodynamics* (Wiley, New York, 1999).
27. Rosa, E. B. The self and mutual inductances of linear conductors. *Nat. Bur. Stand.* **4**, 301–344 (1908).
28. Ordal, M. A., Bell, R. J., Alexander, R. W., Long, L. L. Jr. & Querry, M. R. Optical properties of fourteen metals in the infrared and far infrared: Al, Co, Cu, Au, Fe, Pb, Mo, Ni, Pd, Pt, Ag, Ti, V, and W. *App. Optics* **24**, 4493–4499 (1985).

Acknowledgments

In memoriam Prof. Mario Sorolla. Effort sponsored by Spanish Government under contracts Consolider “Engineering Metamaterials” CSD2008-00066, TEC2011-28664-C01 and TEC2011-28664-C02. V.T. acknowledges funding from Universidad Pública de Navarra. P.R.-U. is sponsored by the Government of Navarra under funding program “Formación de tecnólogos” 055/01/11. M.N.-C. is supported by the Imperial College Junior Research Fellowship. M.B. acknowledges funding by the Spanish Government under the research contract program Ramón y Cajal RYC-2011-08221.

Author contributions

M.B. and M.S. conceived the idea and supervised the study. V.T., R.O. and P.R.-U. performed the experiment and data analysis. A.G. fabricated the samples. V.T. and R.O. contributed to the numerical results. V.T., R.O. and P.R.-U. contributed to the equivalent circuit analysis. V.T., R.O., P.R.-U., A.M., M.N.-C. and M.B. contributed to the discussion. V.T., R.O., M.N.-C. and M.B. wrote the paper.

Additional information

Competing financial interests: The authors declare no competing financial interests.

How to cite this article: Torres, V. *et al.* Mid-infrared plasmonic inductors: Enhancing inductance with meandering lines. *Sci. Rep.* **4**, 3592; DOI:10.1038/srep03592 (2014).



This work is licensed under a Creative Commons Attribution-NonCommercial-ShareAlike 3.0 Unported license. To view a copy of this license, visit <http://creativecommons.org/licenses/by-nc-sa/3.0>